PHYSICAL REVIEW MATERIALS **2**, 075601 (2018)

Searching for crystal-ice domains in amorphous ices

Fausto Martelli,[1,2,*] Nicolas Giovambattista,[3,4] Salvatore Torquato,[2] and Roberto Car[2]
[1] *IBM Research, Hartree Centre, Daresbury WA4 4AD, United Kingdom*
[2] *Department of Chemistry, Princeton University, Princeton, New Jersey 08544, USA*
[3] *Department of Physics, Brooklyn College of the City University of New York, Brooklyn, New York 11210, USA*
[4] *The Graduate Center of the City University of New York, New York, New York 10016, USA*

(Received 7 May 2018; published 2 July 2018)

We employ classical molecular dynamics simulations to investigate the molecular-level structure of water during the isothermal compression of hexagonal ice (I*h*) and low-density amorphous (LDA) ice at low temperatures. In both cases, the system transforms to high-density amorphous ice (HDA) via a first-order-like phase transition. We employ a sensitive local order metric (LOM) [F. Martelli *et al.*, Phys. Rev. B **97**, 064105 (2018)] that can discriminate among different crystalline and noncrystalline ice structures and is based on the positions of the oxygen atoms in the first- and/or second-hydration shell. Our results confirm that LDA and HDA are indeed amorphous, i.e., they lack polydispersed ice domains. Interestingly, HDA contains a small number of domains that are reminiscent of the unit cell of ice IV, although the hydrogen-bond network (HBN) of these domains differs from the HBN of ice IV. The presence of ice-IV-like domains provides some support to the hypothesis that HDA could be the result of a detour on the HBN rearrangement along the I*h*-to-ice-IV pressure-induced transformation. Both nonequilibrium LDA-to-HDA and I*h*-to-HDA transformations are two-step processes where a small distortion of the HBN first occurs at low pressures and then, a sudden, extensive rearrangement of hydrogen bonds at the corresponding transformation pressure follows. Interestingly, the I*h*-to-HDA and LDA-to-HDA transformations occur when LDA and I*h* have similar local order, as quantified by the site-averaged LOMs. Since I*h* has a perfect tetrahedral HBN while LDA does not, it follows that higher pressures are needed to transform I*h* into HDA than that for the conversion of LDA to HDA. In correspondence with both first-order-like phase transitions, the samples are composed of a large HDA cluster that percolates within the I*h*/LDA samples. Our results shed light on the debated structural properties of amorphous ices and indicate that the kinetics of the I*h*-to-HDA and LDA-to-HDA transformations require an in-depth inspection of the underlying HBN. Such investigation is currently ongoing.

DOI: 10.1103/PhysRevMaterials.2.075601

I. INTRODUCTION

At deeply supercooled conditions, water exhibits polyamorphism, i.e., it exists in more than one amorphous solid state. The most common forms of glassy water are the low-density amorphous (LDA) and the high-density amorphous (HDA) ice [1–6]. LDA is likely the most abundant form of ice in the universe and can be produced, for example, by rapid quenching of liquid water at atmospheric pressure [7]. The LDA that is thought to exist in space forms by condensation of water from the gas phase onto cold surfaces [8,9]. HDA can be produced, for example, by pressure-induced amorphization (PIA) of hexagonal ice (I*h*) or by isothermal compression of LDA [10–13]. Remarkably, LDA and HDA can be interconverted by isothermal compression/decompression at $T = 130 - 140$ K [10,14,15] and by isobaric heating at different pressures [14,16,17]. A third form of glassy water, a very high-density amorphous (VHDA) ice, has been identified at very high pressures [18]. We note that experiments show that LDA and HDA can be separated into subfamilies of amorphous structures, e.g., LDA_I and LDA_{II} for LDA [19], and unannealed HDA (uHDA) and expanded HDA (eHDA) for the case of HDA [5,6,20,21]. However, this distinction is less clear in computer simulations and, therefore, we refer to glassy water as either LDA or HDA.

At small length scales, LDA and HDA are structurally very different. LDA has well-separated first- and second-hydration shells, with nearest neighbors arranged in a tetrahedral-like local structure. In this regard, the structure of LDA is reminiscent of the local structure of I*h*. By contrast, HDA has interstitial molecules populating the space between the first- and the second-hydration shells, thus acquiring distorted local configurations similar to liquid-water configurations at ambient conditions [16,22–26]. LDA and HDA also differ in terms of the hydrogen-bond network (HBN). The HBN of LDA is dominated by five-, six-, and sevenfold rings, in contrast to HDA whose HBN includes a significant fraction of longer member rings to accommodate the larger density of the system ($\sim 20 - 25\%$ larger than LDA) [27]. Despite these local structural differences, at large length scales the two glass forms are nearly hyperuniform, i.e., they possess a similar degree of suppression of large-scale density fluctuations, indicating that they should possess similar large-scale structures and large-scale translational order [28].

LDA and HDA were discovered more than 30 years ago [1]. Yet, the nature of LDA and HDA, and the associated LDA-to-HDA first-order-like phase transition, remain highly debated. It

---

[*] Corresponding author: fausto.martelli@ibm.com

has been suggested that LDA and HDA are thermodynamically connected with the liquid, e.g., by isobaric cooling/heating [10]. Elsewhere, HDA was interpreted to be a collapsed HBN of water molecules, unrelated to the liquid state [29–31]. It has also been suggested that HDA may contain nanometer-scale ice domains. After all, HDA transforms to ice IV at very high pressure [32,33] and it can be formed by compression of I*h*. Unfortunately, experimental studies that focus on the structure of LDA and HDA at intermediate length scales are challenging [6]. Computer-simulation studies that describe the structure of LDA and HDA, especially the search for the presence of icelike domains, are rare.

In this article, we perform out-of-equilibrium classical molecular dynamics (MD) simulations to study the structural order during the I*h*-to-HDA and LDA-to-HDA transformations; in particular, we look for traces of crystalline domains during these process. We will refer to the HDA produced upon compression of I*h* as $\mathrm{HDA}_{\mathrm{I}h}$, and to the HDA obtained upon compression of LDA as $\mathrm{HDA}_{\mathrm{LDA}}$. We probe the short- and intermediate-range order during these transformations using a recently developed local order metric (LOM). The LOM measures the degree of order present in the neighborhood of an atomic or molecular site in a condensed medium [34]. The LOM is endowed with a high-resolving power [34–36] and allows one to look for specific ordered domains defined by the location of selected atoms (e.g., water oxygens) in a given reference structure. Typically, the reference structure is taken to be the local structure of a perfect crystalline phase.

We have looked for signatures of ices I*h*, cubic (I*c*), II, III, IV, V, VI, and VII, in LDA and HDA. According to our analysis, both amorphous ices lack polydispersed ordered crystalline domains. However, we find that the oxygens of a few water molecules in HDA are arranged as in the unit cell of ice IV. This observation provides support to the picture proposed in Ref. [37], where the collapse of the HBN of I*h* occurring upon isothermal compression does not lead to ice IV, but to HDA, and is hence considered a "derailed" state along the I*h*-to-ice-IV pathway. Our observation is also consistent with the transformation of HDA to ice IV reported in experiments at very high pressures [32,33]. On the other hand, we also find that the HBN connecting the water molecules in these ice-IV-like domains in HDA *differs* from the HBN in the unit cell of ice IV.

Our analysis indicates that the I*h*-to-HDA transformation is a two-step process in which, first, compression causes a continuous distortion of the ordered HBN of I*h*. This continuous distortion of the HBN is then followed by a sudden extensive rearrangement of the HBN that occurs in correspondence with the I*h*-to-HDA first-order-like phase transition. A similar two-step process occurs during the LDA-to-HDA transformation. In this case, however, although LDA and I*h* acquire similar tetrahedral configurations, the LDA-to-HDA transformation is milder than the I*h*-to-HDA transformation, and it occurs at lower pressures. We notice that the second-hydration shell in I*h* is well ordered. Conversely, the second-hydration shell in LDA describes an "open cage" with a disordered HBN and, therefore, is less rigid. Hence, we relate the lower transformation pressure in LDA, relative to I*h*, to the lower rigidity of the second-hydration shell in LDA compared to I*h*. We complement our analysis by performing a clustering analysis of local environments at different pressures and show that both LDA-to-HDA and I*h*-to-HDA transformations are reminiscent of spinodal decompositions, without nucleation and growth of HDA within LDA/I*h*.

The article is organized as follows. In Sec. II, we provide a brief definition of the LOM employed in this work. In Secs. III A and III B, we discuss the short- and intermediate-range order, respectively, in both LDA and HDA. In Sec. III C, we discuss the spatial aggregation (clusters) of LDA-, HDA-, and I*h*-like molecules during the LDA-to-HDA and I*h*-to-HDA transformations. Conclusions and final remarks are presented in Sec. IV.

II. THE LOCAL ORDER METRIC

In this section, we briefly describe the local order metric employed in this work. The details of the numerical algorithm can be found in Ref. [34]. The local environment of an atomic site j in a snapshot of a molecular dynamics or Monte Carlo simulation defines a local pattern formed by M neighboring sites. Typically these include the first and/or second neighbors of the site j. There are N local patterns, one for each atomic site j in the system. The local reference structure is the set of the same M neighboring sites in an ideal lattice of choice, the spatial scale of which is fixed by setting its nearest-neighbor distance equal to d, the average equilibrium value in the system of interest. For a given orientation of the reference structure and a given permutation $\mathcal{P}$ of the pattern indices, we define the LOM $S(j)$ as the maximum overlap between pattern and reference structure in the j neighborhood by

$$S(j) = \max_{\theta,\phi,\psi;\mathcal{P}} \left\{ \prod_{i=1}^{M} \exp\left(- \frac{\left| \mathbf{P}^{j}_{i\mathcal{P}} - \mathbf{A}^{j}\mathbf{R}^{j}_{i} \right|^{2}}{2\sigma^{2}M} \right) \right\}, \tag{1}$$

where θ,ϕ, and ψ are Euler angles, $\mathbf{P}^{j}_{i\mathcal{P}}$ and $\mathbf{R}^{j}_{i}$ are the pattern and the reference position vectors in the laboratory frame of the M neighbors of site j, respectively, and $\mathbf{A}^{j}$ is an arbitrary rotation matrix about the pattern centroid. The parameter σ controls the spread of the Gaussian functions ($\sigma = d/4$ in this work, where d is the characteristic length of the local pattern). The LOM satisfies the inequalities $0 \lesssim S(j) \leqslant 1$. The two limits correspond, respectively, to a local pattern with randomly distributed points [$S(j) \to 0$] and to an ordered local pattern perfectly matching the reference [$S(j) \to 1$]. We also define global order parameters based on $S(j)$, as the average score function S:

$$S = \frac{1}{N} \sum_{j=1}^{N} S(j). \tag{2}$$

To improve statistics, the score functions are also averaged over 10 independent (LDA-to-HDA and I*h*-to-HDA) trajectories.

III. RESULTS

Our study is based on classical molecular dynamics simulations of a system of $N = 8192$ water molecules described by the classical TIP4P/2005 interaction potential [38]. This water model is able to reproduce relatively well the structures of LDA and HDA at low temperatures [26]. Computer-simulation details and a description of the protocols employed in this work

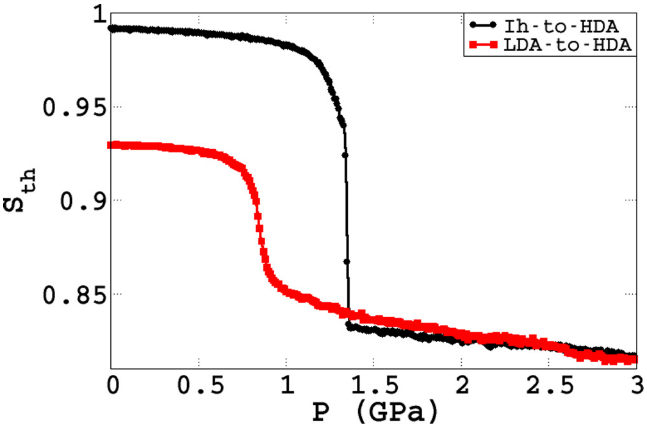

FIG. 1. Local tetrahedrality during the I*h*-to-HDA (black circles) and LDA-to-HDA (red squares) transformations. S_{th} is the score function defined using a regular tetrahedron as a reference structure. In both transformations, compression at low pressures leads to a continuous decrease in local tetrahedrality. The sudden jump in S_{th} at $p \sim 0.83$ GPa (LDA) and $p \sim 1.36$ GPa (I*h*) coincides with the sharp transformation of the system to HDA [39].

are provided in Ref. [39]. Briefly, we prepare LDA by cooling an equilibrium liquid from 240 to 80 K, with a cooling rate of 1 K/ns. HDA is obtained by isothermal compression of I*h* and LDA at $T = 80$ K. During the compression of I*h* and LDA, the pressure is increased from ambient to 3.0 GPa at a pace of 0.01 GPa/ns. For the water model considered, at the present cooling and compression rates, the I*h*-to-HDA transformation occurs at $p = 1.35$ GPa, while the LDA-to-HDA transformation occurs at $0.83 \lesssim p \lesssim 0.93$ GPa [39]. All results reported in this work are averaged over 10 independent trajectories.

A. Short-range order: Local tetrahedrality

In this section, we discuss the local structure of water during the LDA-to-HDA and I*h*-to-HDA transformation at the level of the first-hydration shell. Experiments and computer simulations indicate that the local structure of I*h* and LDA is tetrahedral, i.e., a given molecule is located at the center of a tetrahedron and its four nearest neighbors are roughly located at the corner of such a tetrahedron. Therefore, in order to probe the short-range order of water during the LDA-to-HDA and I*h*-to-HDA transformations, we consider a LOM defined using, as a reference structure, a regular tetrahedron. The resulting score function S_{th} is shown in Fig. 1 for the compression of I*h* (black circles) and LDA (red squares). At low applied pressures, both I*h* and LDA acquire high values of S_{th}, reflecting the nearly perfect regular tetrahedrality of I*h* and LDA. Upon compressing the samples, S_{th} slightly decreases as the local tetrahedral structures get more and more distorted. The transformation of LDA and I*h* to HDA occurs, respectively, at $0.83 \lesssim p \lesssim 0.93$ and $1.35 \lesssim p \lesssim 1.36$ GPa. Accordingly, Fig. 1 shows that at these pressures, S_{th} decays sharply, with the change in S_{th} being more abrupt for the case of I*h* than for LDA.

The behavior of S_{th} in Fig. 1 is consistent with the evolution of the tetrahedral order parameter q [40,41] during the I*h*-to-HDA and LDA-to-HDA transformations reported in Ref. [39]. In particular, it was found that both I*h*-to-HDA and LDA-to-HDA transformations occur when the tetrahedral order parameter reaches a specific critical value, $q \sim 0.32$. Similarly, Fig. 1 indicates that both transformations occur when S_{th} reaches the critical value $S_{\mathrm{th}} \sim 0.91$ and $S_{\mathrm{th}} \sim 0.94$ in LDA and I*h*, respectively. This strongly suggests that the transformation of LDA and I*h* to HDA have a common origin: the rearrangement of the HBN [42] that occurs at $S_{\mathrm{th}} \sim 0.91 - 0.94$. This also explains why the transformation pressure is higher for I*h* than for LDA. Specifically, the HBs in I*h* are more linear (and thus stronger [22,43]) than in LDA and, hence, in order to distort the HBN to the point that $S_{\mathrm{th}} \sim 0.91 - 0.94$, one needs to apply larger pressures to I*h* than to LDA.

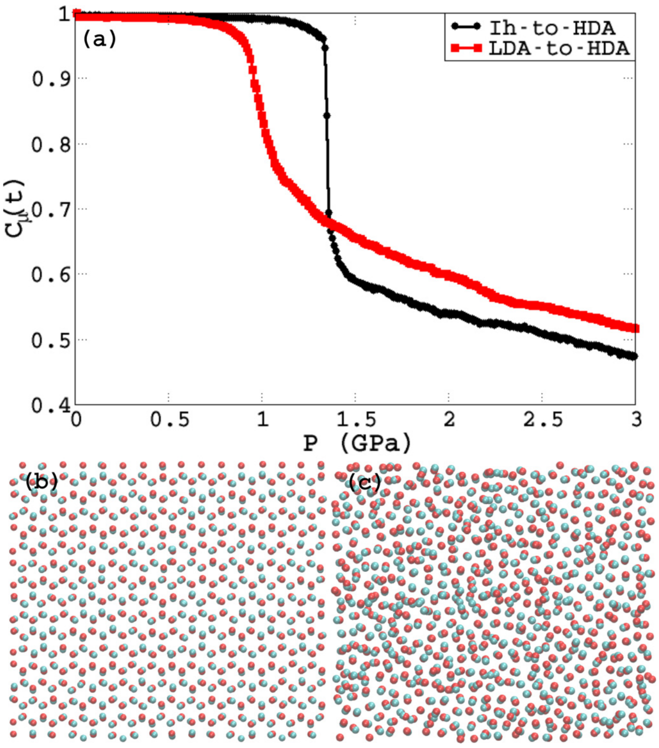

FIG. 2. (a) Water dipole moment correlation function $C_\mu(p)$ as a function of pressure during the I*h*-to-HDA (black circles) and LDA-to-HDA (red squares) transformations. (b) Snapshot of a 4-Å-thick slice of I*h* at $p = 0$ GPa. (c) Snapshot of a 4-Å-thick slice of HDA at $p = 3.0$ GPa. Red spheres represent the oxygen atoms and the cyan spheres indicate the position of the corresponding dipole endpoint.

To shed light on the microscopic origin of the LDA-to-HDA and I*h*-to-HDA transformations, we also study the normalized molecular dipole correlation function, $C_\mu(p) = \langle \mu(p) \cdot \mu(0) \rangle$, where $\mu(0)$ is the molecular dipole vector at pressure $p = 0$ GPa, $\mu(p)$ is the molecular dipole vector at pressure p, and $\langle \cdot \rangle$ indicates an average over all molecules in the system. Figure 2(a) shows the profile of $C_\mu(p)$ for the I*h*-to-HDA transformation (black circles) and for the LDA-to-HDA transformation (red squares). At low pressures, it shows only a mild decay upon compression. In correspondence with both transition pressures, $C_\mu(p)$ shows a marked drop, indicating that water molecules rotate, causing a rearrangement in the HBN. In particular, the drop in $C_\mu(p)$ for the transformation of I*h* is larger than the drop in $C_\mu(p)$ for the transformation of LDA. As an example, we include in Figs. 2(b) and 2(c) two

TABLE I. Score function S_α (averaged over 10 independent trajectories) for LDA at $p = 0.1$ MPa and HDA at $p = 3.0$ GPa. S_α is the score function defined using, as a reference structure, the first and/or second shell of ice $\alpha =$ I*h*, I*c*, II–VII. There are M water oxygens in these reference structures. Included are the number of crystallites, N_{cryst}, found in LDA and HDA for the ices studied (see text).

Ice α	M	Shells	N_{cryst} (LDA)	S_α (LDA)	N_{cryst} (HDA)	S_α (HDA)
I*h*	12	2nd	0	0.416 ± 0.085	0	0.581 ± 0.039
I*c*	12	2nd	0	0.331 ± 0.081	0	0.557 ± 0.039
II	11	1st and 2nd	0	0.389 ± 0.054	0	0.562 ± 0.049
III	11	1st and 2nd	0	0.403 ± 0.015	0	0.592 ± 0.054
IV	13	1st and 2nd	0	0.368 ± 0.069	114 ± 18	0.665 ± 0.054
V	14	1st and 2nd	0	0.327 ± 0.021	0	0.461 ± 0.054
VI	11	1st and 2nd	0	0.204 ± 0.033	0	0.404 ± 0.054
VII	19	1st and 2nd	0	0.312 ± 0.028	0	0.469 ± 0.054

snapshots of a 4-Å-thick slice of I*h* at $p = 0$ GPa and of HDA at $p = 3$ GPa. The red spheres correspond to oxygen atoms, while the cyan spheres correspond to the positions of the endpoint of the molecular dipoles. One can appreciate how the ordered pattern in the dipoles distribution on I*h* is broken in HDA.

B. Intermediate-range order: Searching for ice I*h*, I*c*, and II–VII

In this section, we focus on the local structure of water at intermediate length scales. Specifically, we study the structure of water during the LDA-to-HDA and I*h*-to-HDA transformations at the level of the second-hydration shell. This allows us to compare the structure of LDA and HDA relative to the structure of I*h* as well as intermediate- and high-pressure ices. Water can acquire more than 18 different crystalline forms [44]. However, at the temperature ($T = 80$ K) and pressures ($0 \leqslant p \leqslant 3$ GPa) studied here, the system can only visit the stability regions of the phase diagram of ice corresponding to I*h* and I*c*, as well as ices II–VII. Accordingly, we focus on the score function S_α associated to ice $\alpha =$ I*h*, I*c*, II, III, IV, V, VI, and VII, and defined using, as a reference structure, the first- and/or second-hydration shell of the corresponding ice.

Table I shows the value of the score functions S_α for the cases of LDA at $p = 0.1$ MPa and HDA at $p = 3.0$ GPa. In the case of HDA, we obtain similar values of S_α for $\mathrm{HDA}_{\mathrm{LDA}}$ and $\mathrm{HDA}_{\mathrm{I}h}$. Also included in Table I are the number of crystallites found in LDA and HDA. For a given ice α, we define a crystallite as a water oxygen j for which the LOM $S_\alpha(j) > S_0$, plus its M neighbors used in the reference structure of the corresponding LOM. S_0 is a cutoff reference value. In this work, we chose $S_0 = 0.8$ because we find that for all ices studied, $S_\alpha(j) > 0.8$. As an example, we include in Figs. 3(a)–3(c) the probability distribution of $S_\alpha(j)$ in LDA (black) and HDA (red), for the cases $\alpha =$ II, III, and IV. In Figs. 3(a)–3(c), we also report the distributions of S_α obtained in samples of ice II, III, and IV computed in their thermodynamic stability regions (green) [45]. As shown in Table I, these are among the ices with larger values of the score function S_α in HDA.

There are two main points that follow from our MD simulations. On one hand, (i) LDA and HDA do not contain any crystalline domain, i.e., $S_\alpha(j) < 0.8$ for all atoms in the systems (in the case of HDA, this holds for HDA prepared by compression of ice I*h* and LDA). On the other hand, (ii) there are a few spread traces of ice IV in HDA. Specifically, the tail of the distribution of the LOM $S_{\mathrm{IV}}(j)$ for HDA clearly extends to values larger than 0.8 [Fig. 3(c)], which is not the case for other ices [see, e.g., the cases of ice II and III in Figs. 3(a) and 3(b)]. In particular, the distribution of $S_{\mathrm{IV}}(j)$ in HDA partially overlaps with the corresponding distribution in a pure sample of ice IV. We stress that the number of ice-IV-like domains is rather small; there are only 114 ice-IV-like centers in HDA at $p = 3.0$ GPa for the case $S_0 = 0.8$. Such molecules have a LOM $S_{\mathrm{IV}}(j) \sim S_0 = 0.8$, indicating highly distorted environments. The absence of crystallites of ice I*h*, I*c*, and II–VII and the very small amount of ice-IV-like crystallites enable us to conclude that HDA and LDA are indeed true amorphous structures. Our conclusion is strengthened further by inspecting the HBN of the ice-IV-like crystallites, as discussed in the next section.

1. Score function based on ice IV

The presence of ice-IV-like molecules in HDA is consistent with the crystallization of HDA into ice IV reported in high-pressure experiments [32,33]. Our results also provide

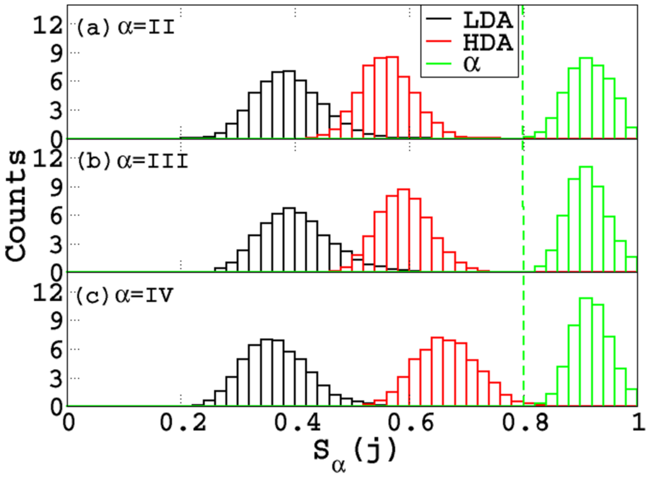

FIG. 3. Histogram of the LOM $S_\alpha(j)$, given by Eq. (1) calculated using, as a reference, the unit cells of ice (a) $\alpha =$ II, (b) $\alpha =$ III, and (c) $\alpha =$ IV for LDA (black) and for $\mathrm{HDA}_{\mathrm{I}h}$ (red) at $p = 0.01$ and $p = 3.0$ GPa, respectively. The green distributions represent the histograms for the corresponding bulk ices computed at the following thermodynamic conditions [45]: $T = 210$ K and $p = 4$ GPa for ice II, and $T = 250$ K and $p = 3$ GPa for ice III and IV. The green line emphasizes the value $S = 0.8$ used as a cutoff to identify icelike environments.

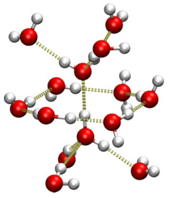

FIG. 4. Unit cell of ice IV. The dashed lines represent the hydrogen bonds.

support to the hypothesis that HDA may be an intermediate, "derailed" glassy state formed during the Ih-to-ice IV transformation [37]. However, we note that the HBN of the ice-IV domains found in HDA differs from the HBN in ice IV. Specifically, the basic structure of ice IV is shown in Fig. 4 and is characterized by a water hexagon pierced by a donor-acceptor hydrogen bond. This donor-acceptor HB is the origin of the interpenetrating HBN that characterizes ice IV [46]. We have inspected the topology of the HBN of all 114 ice-IV-like domains in HDA at $p = 3$ GPa and found no indication of the donor-acceptor HB shown in Fig. 4. Hence, the ice-IV-like domains should not be interpreted as nanoscopic crystals, but as disordered local domains in which the second shell of neighbors of the central molecule resembles a distorted second-hydration shell of ice IV. Indeed, network interpenetration severely constrains the configurational disorder of water's HBN and is discouraged by entropy. Thus, network interpenetration does not usually occur in disordered structures, such as the amorphous ices. Interestingly, when network interpenetration occurs, HDA does transform into ice IV, as experimentally observed [32,47]. It follows from our results that although HDA may be considered as a derailed state along the Ih-to-IV transformation, the microscopic mechanisms involved in this transformation require further investigations [37].

In order to delve deeper into the details of the ice-IV character of HDA, we show in Fig. 5(a) the pressure dependence of $S_{\rm IV}$ during the Ih-to-HDA transformation. The $S_{\rm IV}$ is defined using, as a reference, the unit cell of ice IV shown in Fig. 5(a). For comparison, we also include $S_{\rm IV}$ during the LDA-to-HDA transformation. Along both transformations, the ice-IV character of both Ih and LDA increases smoothly with pressure and, in correspondence with both nonequilibrium transformations, $S_{\rm IV}$ shows a sudden increase, from $S_{\rm IV} = 0.46 - 0.47$ to $S_{\rm IV} = 0.64 - 0.66$. Interestingly, as for the short-range $S_{\rm th}$, both Ih and LDA need to acquire a similar value of $S_{\rm IV}$ before being converted to HDA, i.e., $S_{\rm IV} \sim 0.52$ at the corresponding transition pressures. This observation further explains why the transformation pressure is higher for Ih than for LDA, and indicates that such difference is an effect that also extends beyond the first-hydration shell. We also note that the continuous increment of the ice-IV character with the increasing pressure in HDA is a further indication of the HDA-to-ice-IV transformation that may occur at higher pressures [32,33].

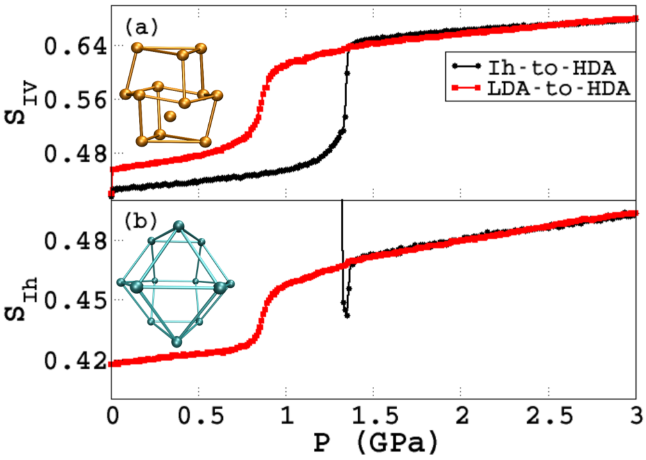

FIG. 5. (a) Score function $S_{\rm IV}$ during the Ih-to-HDA (black) and the LDA-to-HDA (red) transformation. The snapshot represents the reference structure used to compute $S_{\rm IV}$. (b) Score function $S_{{\rm I}h}$ during the Ih-to-HDA (black) and the LDA-to-HDA (red) transformation. The snapshot depicts the reference structure used in the definition of $S_{{\rm I}h}$.

2. Score function based on **I*h***

Considering that LDA and Ih have a similar degree of tetrahedrality (see Fig. 1), one may wonder how similar LDA and Ih are at the level of the second-hydration shell. To address this issue, we study $S_{{\rm I}h}$, i.e., the score function defined using, as a reference structure, the second-hydration shell of ice Ih [see snapshot of Fig. 5(b)]. Figure 5(b) shows $S_{{\rm I}h}$ during the Ih-to-HDA (black line) and LDA-to-HDA (red line) transformations. The values of $S_{{\rm I}h}$ for Ih at low pressures are not shown because they are, as one would expect, close to 1. Remarkably, in correspondence with the Ih-to-HDA first-order-like phase transition, $S_{{\rm I}h}$ acquires a minimum that could be interpreted as the limit of mechanical stability for Ih. Further compression results in a continuous but mild increase in $S_{{\rm I}h}$ within the HDA$_{{\rm I}h}$ state. We note that $S_{{\rm I}h}$ is practically the same for both HDA$_{\rm LDA}$ and HDA$_{{\rm I}h}$, indicating that the average structure of HDA is independent of the recipe followed to prepare HDA.

A comparison of Figs. 1 and 5(b) shows that although LDA and Ih have very similar tetrahedrality (and density), they differ remarkably at the level of the second shell. This is shown in Figs. 6(a) and 6(b) that include, respectively, a representative arrangement of water molecules in the first- and second-hydration shell of Ih and LDA, taken from our MD simulations. The yellow water molecule is the shared vertex of four tetrahedra (emphasized in yellow) that are the source of the high tetrahedrality of both samples. The centers of each of these tetrahedra are occupied by the red water molecules; these four (red) water molecules constitute the first-hydration shell of the central (yellow) molecule. The outer vertices of the (yellow) tetrahedra are occupied by 12 molecules, shown in gray. These molecules constitute the second-hydration shell of the central (yellow) water molecule. The oxygens in the second shell of Ih describe an anticuboctahedron, emphasized by the blue snapshot in Fig. 5(b). A comparison of Figs. 6(a) and 6(b) shows that in the local structure of LDA, one of the four tetrahedra is broken, leading to the opening of the anticuboctahedral cage characteristic of Ih. For comparison, included in Fig. 6(c) is the local structure of ice Ic. The second shell of neighbors of Ic (gray O atoms) describes the Archimedean solid cuboctahedron [48] and differs from the anticuboctahedron in the local

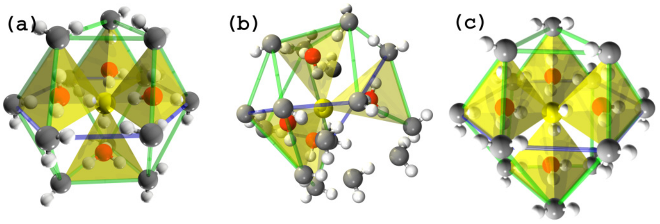

FIG. 6. Local structure of (a) I*h*, (b) LDA, and (c) ice I*c*. The central water molecule is depicted in yellow and is located at the shared vertex of the four tetrahedra depicted in yellow. The water molecules in the first shell of the central (yellow) water molecule are shown in red and are located at the center of the four (yellow) tetrahedra. The water molecules on the second shell of the central (yellow) molecule are depicted in gray and are located at the outer vertices of the (yellow) tetrahedra. In the case of I*h*, the gray molecules describe an anticuboctahedron whose structure is emphasized by the green and blue lines. In the case of LDA, one of the four (yellow) tetrahedra of the anticuboctahedral cage is broken. In the case of I*c*, the second shell of neighbors describes the Archimedean solid cuboctahedron.

structure of ice I*h*. Specifically, the anticuboctahedron (I*h*) is the 27th Johnson solid [49] and differs from the cuboctahedron (I*c*) by a rotation of 120° in one of the four (yellow) tetrahedra [Fig. 6(c)].

C. Clustering analysis

In this section, we describe the structural changes underlying the I*h*-to-HDA and the LDA-to-HDA transformations by looking at the spatial distribution of ice-IV-, ice-I*h*-, LDA-, and HDA-like water molecules through the system. We classify a water molecule j as an I*h*-like molecule if the corresponding LOM $S_{Ih}(j) > S_0$, and as an ice-IV-like molecule if its LOM $S_{IV}(j) > S_0$; otherwise, the molecule is considered to belong to an amorphous ice. The value $S_0 = 0.8$ is chosen because for ices $\alpha =$ I*h* and IV, $S_\alpha(j) > 0.8$, while $S_\alpha(j) < 0.8$ for molecules in LDA and HDA; see Figs. 7 and 3(c). In order to distinguish between LDA- and HDA-like molecules, we consider the LOM $S_{IV}(j)$. As shown in Fig. 3(c), molecules in LDA (HDA) are characterized by approximately $S_{IV}(j) < S_{0'}$ [$S_{IV}(j) > S_{0'}$] with $S_{0'} = 0.58$.

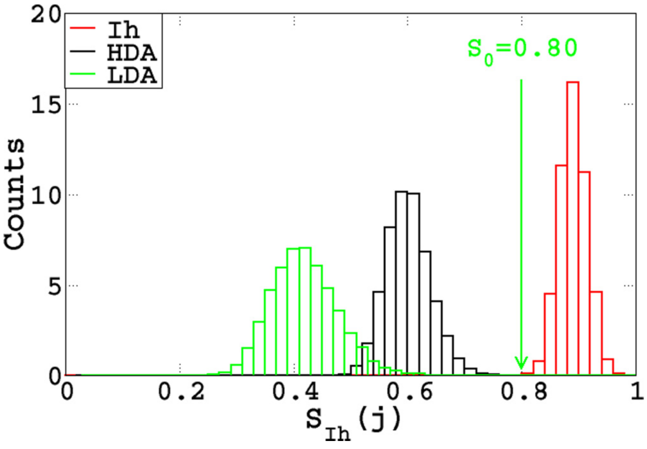

FIG. 7. Histogram of the LOM $S_{Ih}(j)$ [Eq. (1)] calculated using, as a reference, the second shell of neighbors of ice I*h* for HDA (black) at $p = 3.0$ GPa, I*h* (red) at $p = 0.01$ GPa, and LDA (green) at $p = 0.01$ GPa, respectively.

This classification of water molecules allows us to identify clusters of LDA, HDA, ice I*h*, and ice IV. Specifically, two molecules, of the same kind (LDA, HDA, I*h*, and IV), are considered to belong to the same cluster if they form a HB. In this work, we consider that two water molecules form a HB if a H atom of one of these molecules is within a distance $d_{OH} = 2.2$ Å from the O atom of the other molecule; this value of d_{OH} corresponds to the location of the first minimum in the OH radial distribution function of glassy water at $p = 3$ GPa (HDA) [42]. With respect to other HB definitions, this definition leads to a fully formed tetrahedral network in LDA and HDA [42], in agreement with experimental results [50].

1. The I*h-to-HDA transformation*

Figure 8(a) shows the percentage of I*h*-like (black circles) and HDA-like (red squares) molecules during the I*h*-to-HDA transformation for the pressure window $0.4 \leqslant p \leqslant 1.6$ GPa. Similarly, Fig. 8(b) shows the percentage of LDA-like molecules (green diamonds) and ice-IV-like molecules (blue triangles) during the same transformation.

At $p = 0.6$ GPa, the percentage of I*h*-like molecules is large, $\approx 100\% \approx N$, and decreases smoothly upon further compression to $p = 1.34$ GPa. As shown in Figs. 8(a) and 8(b), the decrease in I*h*-like molecules is accompanied by an increase in HDA-like molecules, from ≈0% at 0.6 GPa to ≈ 20% at $p = 1.34$ GPa. We note that at these pressures, the percentage of LDA-like molecules is relatively small (∼1%) and it reaches a maximum at $p = 1.1 - 1.2$ GPa, while there are no ice-IV-like molecules (at $p < 1.34$ GPa). In correspondence with the I*h*-to-HDA transformation at $p = 1.35$ GPa, we observe a significant drop in the percentage of I*h*-like molecules, from ≈ 80% to ≈ 20%, which is accompanied by an increase in the number of HDA-like molecules, from ≈ 20% to ≈ 80%. Such increment also involves the transformation of LDA domains into HDA domains, accounting for the decrease of LDA domains occurring at lower pressures. Interestingly, at $p > 1.35$ GPa, HDA contains a small number of residual, LDA, and IV molecules; e.g., at $p = 1.4$ GPa, there are only ≈ 0.03% molecules of LDA and ice IV. In addition, depending on pressure, specifically HDA_{Ih} may also contain non-negligible amounts of residual ice-I*h* molecules. At $p = 1.6$ GPa, there is an amount of ∼3.5% of I*h*-like molecules, while ice-I*h* molecules are absent at $p = 3$ GPa.

Figures 8(c) and 8(d) show the percentage of clusters associated to LDA, HDA, ice-I*h*, and IV. At pressures below the transformation pressure, the system contains only one I*h* cluster with several, small disconnected HDA-like and LDA-like clusters. Indeed, the largest LDA and HDA clusters are composed of <0.1% of the total number of molecules (at $p < 1.34$ GPa) [Figs. 8(f) and 8(e)]. On the other hand, in correspondence with the I*h*-to-HDA transformation, the number of I*h*-like clusters increases, from ∼0.1% to ≈ 3%, while the number of HDA-clusters reduces to ∼0.1%. As shown in Fig. 8(e), the largest HDA cluster has ≈ 98% molecules and hence it includes most of the molecules in the

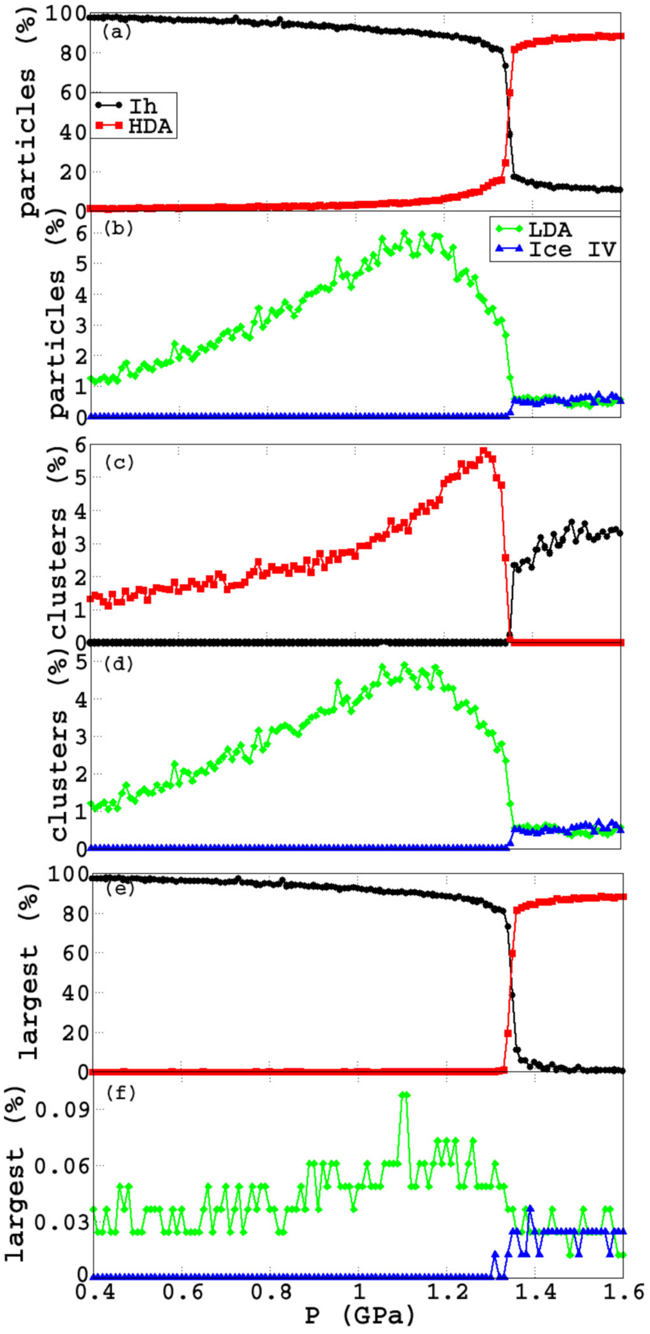

FIG. 8. (a), (b) Percentage of I*h*-like (black circles) and HDA-like (red squares) molecules, and LDA-like (green diamonds) and ice-IV-like (blue triangles) molecules during the I*h*-to-HDA transformation. (c), (d) The corresponding percentage of clusters. (e), (f) The percentage of molecules composing the ice-I*h*, ice-IV, LDA, and HDA clusters.

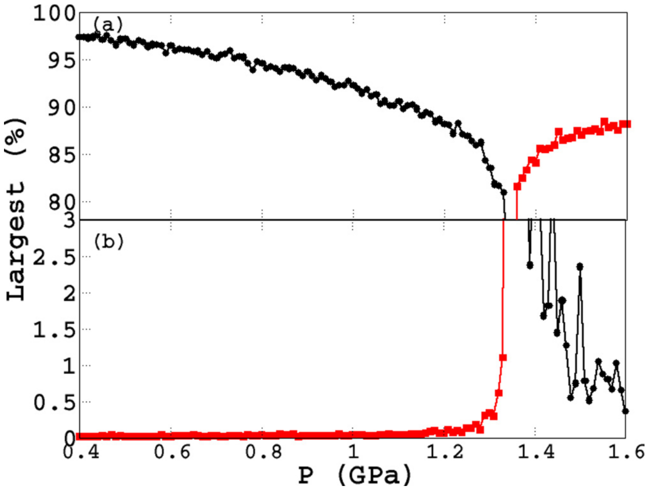

FIG. 9. (a) Percentage of molecules composing the ice-I*h* and HDA clusters in the size window 80% – 100%. (b) Percentage of molecules composing the ice-I*h* and HDA clusters in the size window 0% – 3%.

system, while instead the largest I*h* cluster is small (∼0.1% molecules in size) and, therefore, they are within the HDA matrix. In Fig. 9, we show a zoom of the percentage of the largest I*h* and HDA clusters as a function of the pressure. It is possible to observe that the largest I*h* cluster shrinks at a faster pace than the corresponding HDA cluster increases, indicating that most of the HDA-like domains formed upon increasing the pressure do not populate the largest HDA cluster but, rather, are dispersed on the I*h* sea. It follows that the I*h*-to-HDA transformation is reminiscent of a transformation driven by a spinodal decomposition, rather than by a nucleation-and-growth process as found during crystallization.

2. The LDA-to-HDA transformation

A similar picture holds for the LDA-to-HDA transformation. However, in this case, the transformation is smoother and there are no I*h*-like molecules at any pressure. Accordingly, we only discuss the roles of LDA and HDA during the LDA-to-HDA transformation.

Figure 10(a) shows the percentage of LDA-like (black circles) and HDA-like (red squares) molecules during the LDA-to-HDA transformation for the pressure window $0.01 \leqslant p \leqslant 1.2$ GPa. At $p = 0.01$ GPa, the percentage of LDA-like molecules is large, ≈ 95%, and decreases smoothly upon

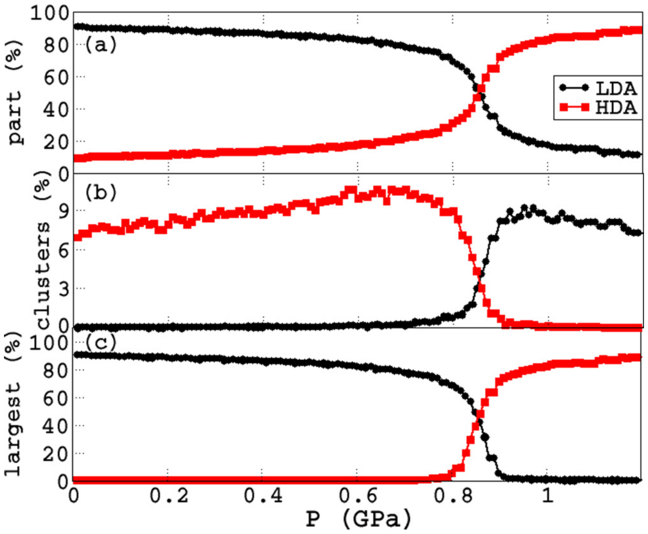

FIG. 10. (a) Percentage of LDA and HDA environments in black and red, respectively, for the LDA-to-HDA transformation. Percentage of (b) number of clusters and of (c) the largest LDA and HDA clusters.

further compression to $p = 0.8$ GPa. As shown in Fig. 10(a), the decrease in LDA-like molecules is accompanied by an increase in HDA-like molecules, from $\approx 10\%$ at $p \sim 0$ GPa to $\approx 30\%$ at $p = 0.80$ GPa. In correspondence with the onset of the LDA-to-HDA transformation at $p = 0.80$ GPa, we observe a significant drop in the number of LDA-like molecules, from $\approx 70\%$ to $\approx 20\%$ at $p = 0.9$ GPa, which is accompanied by an increase in the number of HDA-like molecules, from $\approx 20\%$ to $\approx 80\%$.

Figure 10(b) shows the percentage of clusters associated to LDA and HDA. At pressures below the transformation pressure, the system contains one LDA cluster with several, small disconnected HDA-like clusters that increase in number upon compression, reaching a maximum of $\sim$10% clusters at $p \sim 0.7$ GPa. The largest HDA cluster at $p < 0.8$ GPa is composed of less than 0.1% of the total number of molecules; see Fig. 10(c). On the other hand, in correspondence with the pressure window $0.8 \lesssim p \lesssim 1.0$ GPa, the number of LDA-like clusters increases, from $\approx$1% to $\approx 9\%$, and they decrease at higher pressures, while the percentage of HDA clusters reduces to almost zero. At $p > 0.9$ GPa, this HDA cluster has $N \sim 98\%$ of the total number of molecules in the system while, instead, the largest LDA cluster is small (<0.1% molecules in size) and, therefore, they are within the HDA matrix. It follows that in analogy with the Ih-to-HDA transformation, the LDA-to-HDA transformation is reminiscent of a transformation driven by spinodal decomposition.

IV. SUMMARY AND CONCLUSIONS

We performed classical MD simulations and explored in detail the structure of water at short and intermediate scales during the LDA-to-HDA and Ih-to-HDA transformations. Specifically, by using the LOM developed in Ref. [34], we searched for locally ordered crystalline domains composed of the first and/or second shell of neighbors in the amorphous ices formed during the Ih-to-HDA and the LDA-to-HDA pressure-induced transformations. Our results confirm that LDA and HDA are indeed amorphous, i.e., they lack polydispersed icelike structures. Surprisingly, we find that HDA contains a small number of domains that are reminiscent of ice IV. The presence of ice-IV-like domains provides some support to the hypothesis that HDA could be a derailed state along the Ih-to-ice-IV pathway [37]. However, the HBN of these domains differ from the HBN of ice IV. The ice-IV basic structure includes the interpenetration of two HBNs (Fig. 4). However, interpenetration of HBNs is highly improbable in amorphous structures such as HDA since it constrains the local possible orientations of water molecules and hence it tends to reduce the entropy of the amorphous ice. In our view, since the crystallization to ice IV has been shown to have the lowest activation energy out of all of the possible crystallization pathways around 1 GPa [32,33,47], the transformation of HDA to ice IV is not fully understood and requires further investigation.

By characterizing the structure of water at the first- and second-hydration shells, we also provided some understanding of the differences and similarities in the molecular changes underlying the LDA-to-HDA and Ih-to-HDA transformations. Our results indicate that both nonequilibrium transformations are two-steps processes where, first, a small distortion of the HBN occurs at low pressures and, then, a sudden, extensive rearrangement of HBs at the corresponding transformation pressure occurs. The Ih-to-HDA and LDA-to-HDA transformations occur when LDA and Ih have similar local order, as quantified by various score functions (e.g., S_{IV}, $S_{\mathrm{I}h}$, and S_{th}). Since Ih has a perfect tetrahedral HBN while LDA does not, it follows that higher pressures are needed to distort the HBN of Ih relative to LDA. Accordingly, Ih can resist larger pressures than LDA before collapsing to HDA, as found in experiments [30,31].

From the microscopic point of view, Ih and LDA are structurally similar at small length scales, both being characterized by a nearly perfect regular tetrahedral HBN. Yet, the Ih-to-HDA transformation is sharp, while the LDA-to-HDA transformation is gradual. Our results suggest that the gradualness of the LDA-to-HDA transformation is due to different structural configurations occurring at the level of the second shell of neighbors: Ih has a well-formed anticuboctahedral structure and an ordered HBN (which rearranges rapidly upon compression for this water model), while LDA has an open cage that causes some degree of disorder in the HBN (Fig. 6) (and rearranges more gradually upon compression) [42].

We also find that both Ih-to-HDA and LDA-to-HDA transformations are first-order-like phase transitions occurring via spinodal decomposition in which HDA clusters percolate within the Ih/LDA sample. At pressures below the Ih/LDA-to-HDA transformations, the system consists of a single large cluster of Ih/LDA, composed of most of the molecules in the system, plus HDA clusters, composed of a few water molecules. At pressures above the transformation pressure, the roles of HDA and Ih/LDA are inverted, i.e., the system is composed of a single HDA cluster composed of most of the molecules in the system, and Ih/LDA clusters (depending on whether the starting phase is Ih or LDA) that are composed of a few water molecules.

We conclude by noting that $\mathrm{HDA}_{\mathrm{I}h}$ and $\mathrm{HDA}_{\mathrm{LDA}}$, at $p = 3$ GPa, are practically identical in terms of water structure at the first- and second-hydration shells. However, minor differences in structure seem to exist at lower pressures, closer to the collapse of Ih and LDA to HDA. For example, it follows from Fig. 8(a) that $\mathrm{HDA}_{\mathrm{I}h}$ contains a few, non-negligible number of Ih-like molecules at $p \sim 1.4 - 1.6$ GPa while, not surprisingly, $\mathrm{HDA}_{\mathrm{LDA}}$ does not. This is consistent with the picture proposed in Refs. [5,6], where uHDA (at $p < 1.5$ GPa) is considered to contain Ih crystallites while other HDA forms, such as eHDA, do not. In our case, $\mathrm{HDA}_{\mathrm{I}h}$ is prepared following the same protocol followed in experiments to prepare uHDA and, accordingly, it contains ice Ih at $p \sim 1.5$ GPa. Instead, $\mathrm{HDA}_{\mathrm{LDA}}$ does not contain ice Ih, as is the case of eHDA. In the pressure range $1.4 \lesssim p \lesssim 1.6$ GPa, the Ih clusters in $\mathrm{HDA}_{\mathrm{I}h}$ are small, composed of $< 5 - 10$ molecules.

Our results shed light on the debated structural properties of amorphous ices and indicate that the kinetics of the Ih-to-HDA and LDA-to-HDA transformations requires an in-depth inspection of the underlying HBN. Such investigation is currently ongoing and will be the subject of a forthcoming paper [42].

ACKNOWLEDGMENTS

This work was supported by the STFC Hartree Centre's Innovation Return on Research programme, funded by the Department for Business, Energy and Industrial Strategy. This work was partially supported by the National Science Foundation Award No. CBS-1604504 (N.G.) and a grant of computer time from the City University of New York High Performance Computing Center under NSF Grants No. CNS-0855217, No. CNS-0958379, and No. ACI-1126113. R.C. acknowledges partial support from the U.S. Department of Energy under Award No. DE-SC0008626. S.T. was supported by the National Science Foundation under Award No. DMR1714722.

---

[1] P. G. Debenedetti, Supercooled and glassy water, J. Phys.: Condens. Matter **15**, R1669(R) (2003).

[2] C. A. Angell, Amorphous water, Annu. Rev. Phys. Chem. **55**, 559 (2004).

[3] T. Loerting and N. Giovambattista, Amorphous ices: Experiments and numerical simulations, J. Phys.: Condens. Matter **18**, R919(R) (2006).

[4] O. Mishima and H. E. Stanley, The relationship between liquid, supercooled and glassy water, Nature (London) **396**, 329 (1998).

[5] T. Loerting, V. Fuentes-Landete, P. H. Handlea, M. Seidl, K. Amann-Winkel, C. Gainaru, and R. Bohme, The glass transition in high-density amorphous ice, J. Non-Cryst. Solids **407**, 423 (2015).

[6] K. Amann-Winkel, R. Bohmer, F. Fujara, C. Gainaru, B. Geil, and T. Loerting, Colloquium: Water's controversial glass transitions, Rev. Mod. Phys. **88**, 011002 (2016).

[7] E. Meyer, New method for vitrifying water and other liquids by rapid cooling of their aerosols, J. Appl. Phys. **58**, 663 (1985).

[8] E. F. Burton and W. F. Oliver, Nature (London) **135**, 505 (1935).

[9] P. Jenniskens and D. F. Blake, Structural transitions in amorphous water ice and astrophysical implications, Science **265**, 753 (1994).

[10] O. Mishima, Reversible first-order transition between two H_2O amorphs at ∼0.2 GPa and ∼135 K, J. Chem. Phys. **100**, 5910 (1994).

[11] O. Mishima, L. D. Calvert, and E. Whalley, "Melting ice" I at 77 K and 10 kbar: A new method of making amorphous solids, Nature (London) **310**, 393 (1984).

[12] O. Andersson, Glass-liquid transition of water at high pressure, Proc. Natl. Acad. Sci. USA **108**, 11013 (2011).

[13] T. Loerting, W. Schustereder, K. Winkel, C. G. Salzmann, I. Kohl, and E. Mayer, Amorphous Ice: Stepwise Formation of Very-High-Density Amorphous Ice from Low-Density Amorphous Ice at 125 K, Phys. Rev. Lett. **96**, 025702 (2006).

[14] K. Winkel, M. Bauer, E. Mayer, M. Seidl, M. S. Elsaesser, and T. Loerting, Structural transitions in amorphous H_2O and D_2O: The effect of temperature, J. Phys.: Condens. Matter **20**, 494212 (2008).

[15] K. Winkel, E. S. Elsaesser, E. Mayer, and T. Loerting, Water polyamorphism: Reversibility and (dis)continuity, J. Chem. Phys. **128**, 044510 (2008).

[16] K. Winkel, E. Mayer, and T. Loerting, Equilibrated high-density amorphous ice and its first-order transition to the low-density form, J. Phys. Chem. B **115**, 14141 (2011).

[17] E. L. Gromnitskaya, O. V. Stal'gorova, V. V. Brazhkin, and A. G. Lyapin, Ultrasonic study of the nonequilibrium pressure-temperature diagram of H_2O ice, Phys. Rev. B **64**, 094205 (2001).

[18] T. Loerting, C. Salzmann, I. Kohl, E. Mayer, and A. Hallbrucker, A second distinct structural state of high-density amorphous ice at 77 K and 1 bar, Phys. Chem. Chem. Phys. **3**, 5355 (2001).

[19] K. Winkel, D. T. Bowron, T. Loerting, E. Mayer, and J. L. Finney, Relaxation effects in low density amorphous ice: Two distinct structural states observed by neutron diffraction, J. Chem. Phys. **130**, 204502 (2009).

[20] R. J. Nelmes, J. S. Loveday, T. Strässle, C. L. Bull, M. Guthrie, G. Hamel, and S. Klotz, Annealed high-density amorphous ice under pressure, Nat. Phys. **2**, 414 (2006).

[21] T. Loerting, K. Winkel, M. Bauer, C. Mitterdorfer, P. H. Handle, E. Mayer, J. L. Finney, and D. Bowron, How many amorphous ices are there?, Phys. Chem. Chem. Phys. **13**, 8783 (2011).

[22] B. Santra, R. A. DiStasio Jr., F. Martelli, and R. Car, Local structure analysis in ab initio liquid water, Mol. Phys. **113**, 2829 (2015).

[23] C. A. Tulk, C. J. Benmore, L. Urquidi, D. D. Klug, J. Neuefeing, B. Tomberli, and P. A. Egelstaff, Structural studies of several distinct metastable forms of amorphous ice, Science **297**, 1320 (2002).

[24] J. L. Finney, A. Hallbrucker, I. Kohl, A. K. Soper, and D. T. Bowron, Structures of High and Low Density Amorphous Ice by Neutron Diffraction, Phys. Rev. Lett. **88**, 225503 (2002).

[25] A. K. Soper and M. A. Ricci, Structures of High-Density and Low-Density Water, Phys. Rev. Lett. **84**, 2881 (2000).

[26] J. Wong, D. A. Jahn, and N. Giovambattista, Pressure-induced transformations in glassy water: A computer simulation study using the TIP4P/2005 model, J. Chem. Phys. **143**, 074501 (2015).

[27] R. Martoňák, D. Donadio, and M. Parrinello, Evolution of the structure of amorphous ice: From low-density amorphous through high-density amorphous to very high-density amorphous ice, J. Chem. Phys. **122**, 134501 (2005).

[28] F. Martelli, S. Torquato, N. Giovambattista, and R. Car, Large-Scale Structure and Hyperuniformity of Amorphous Ices, Phys. Rev. Lett. **119**, 136002 (2017).

[29] J. S. Tse, D. D. Klug, C. A. Tulk, I. Swainson, E. C. Sensson, C.-K. Loong, V. Shapakov, V. R. Belosludov, R. V. Belosludov, and Y. Kawazoe, The mechanism of pressure-induced amorphization of ice I_h, Nature (London) **400**, 647 (1999).

[30] G. P. Johari, On the amorphization of hexagonal ice, the nature of water's low-density amorph, and the continuity of molecular kinetics in supercooled water, Phys. Chem. Chem. Phys. **2**, 1567 (2000).

[31] G. P. Johari and O. Andersson, Mechanisms for pressure- and time-dependent amorphization of ice under pressure, Phys. Rev. B **70**, 184108 (2004).

[32] C. G. Salzmann, T. Loerting, T. Kohl, E. Mayer, and A. Hallbrucker, Pure ice IV from high-density amorphous ice, J. Phys. Chem. B **106**, 5587 (2002).

[33] C. G. Salzmann, E. Mayer, and A. Hallbrucker, Effect of heating rate and pressure on the crystallization kinetics of high-density

amorphous ice on isobaric heating between 0.2 and 1.9 GPa, Phys. Chem. Chem. Phys. **6**, 5156 (2004).

[34] F. Martelli, H.-Y. Ko, E. C. Oğuz, and R. Car, Local-order metric for condensed phase environments, Phys. Rev. B **97**, 064105 (2018).

[35] F. Martelli, H.-Y. Ko, C. C. Borallo, and G. Franzese, Structural properties of water confined by phospholipid membranes, Front. Phys. **13**, 136801 (2018).

[36] B. Santra, H.-Y. Ko, Y. W. Yeh, F. Martelli, I. Kaganovich, Y. Raitses, and R. Car, Root-growth of boron nitride nanotubes: Experiments and *ab initio* simulations, arXiv:1803.11374.

[37] J. J. Shephard, S. Ling, G. C. Sosso, A. Michaelides, B. Slater, and C. G. Salzmann, Is high-density amorphous ice simply a "derailed" state along the ice I to ice IV pathway?, J. Phys. Chem. Lett. **8**, 1645 (2017).

[38] J. L. F. Abascal and C. Vega, Pressure-induced transformations in glassy water: A computer simulation study using the TIP4P/2005 model, J. Chem. Phys. **123**, 234505 (2005).

[39] J. Engstler and N. Giovambattista, Heating- and pressure-induced transformations in amorphous and hexagonal ice: A computer simulation study using the TIP4P/2005 model, J. Chem. Phys. **147**, 074505 (2017).

[40] P.-L. Chau and J. Hardwick, A new order parameter for tetrahedral configurations, Mol. Phys. **93**, 511 (1998).

[41] J. R. Errington and P. G. Debenedetti, Relationship between structural order and the anomalies of liquid water, Nature (London) **409**, 318 (2001).

[42] F. Martelli and N. Giovambattista, (unpublished).

[43] B. Santra, J. Klimeš, D. Alfé, A. Tkatchenko, B. Slater, A. Michaelides, R. Car, and M. Scheffler, Hydrogen Bonds and Van Der Waals Forces in Ice at Ambient and High Pressures, Phys. Rev. Lett. **107**, 185701 (2011).

[44] T. Bartles-Rausch, V. Bergeron, J. H. E. Cartwright, R. Escribano, J. L. Finney, H. Grothe, P. J. Gutirrez, J. Haapala, W. F. Fuchs, J. B. C. Pettersson, S. D. Price, C. I. Sainz-Daz, D. J. Stokes, G. Strazzulla, E. S. Thomson, H. Trinks, and N. Uras-Aytemiz, Ice structures, patterns, and processes: A view across the icefields, Rev. Mod. Phys. **84**, 885 (2012).

[45] M. M. Conde, M. A. Gonzalez, J. F. L. Abascal, and C. Vega, Determining the phase diagram of water from direct coexistence simulations: The phase diagram of the TIP4P/2005 model revisited, J. Chem. Phys. **139**, 154505 (2013).

[46] H. Engelhardt and B. Kamb, Structure of ice IV, a metastable high-pressure phase, J. Chem. Phys. **75**, 5887 (1981).

[47] C. G. Salzmann, I. Kohl, T. Loerting, E. Mayer, and A. Hallbrucker, Pure ices IV and XII from high-density amorphous ice, Can. J. Phys. **81**, 25 (2003).

[48] P. R. Cromwell, *Polyhedra* (Cambridge University Press, New York, 1999).

[49] N. W. Johnson, Convex polyhedra with regular faces, Can. J. Math. **18**, 169 (1966).

[50] C. Lin, J. S. Smith, S. V. Sinogeikin, and G. Shen, Experimental evidence of low-density liquid water upon rapid decompression, Proc. Natl. Acad. Sci. U.S.A. **115**, 2010 (2018).